High-resolution adaptive imaging of a single atom

J. D. Wong-Campos*, K. G. Johnson, B. Neyenhuis, J. Mizrahi and C. Monroe

Optical imaging systems are used extensively in the life and physical sciences because of their ability to non-invasively capture details on the microscopic and nanoscopic scales. Such systems are often limited by source or detector noise, image distortions and human operator misjudgement. Here, we report a general, quantitative method to analyse and correct these errors. We use this method to identify and correct optical aberrations in an imaging system for single atoms and realize an atomic position sensitivity of ~0.5 nm Hz$^{-1/2}$ with a minimum uncertainty of 1.7 nm, allowing the direct imaging of atomic motion. This is the highest position sensitivity ever measured for an isolated atom and opens up the possibility of performing out-of-focus three-dimensional particle tracking, imaging of atoms in three-dimensional optical lattices or sensing forces at the yoctonewton (10^{-24} N) scale.

The optical imaging of isolated emitters, such as individual molecules[1,2], optically active defects in solids[3], fluorescent dyes in a solution[4] or trapped atoms[5,6], relies on efficient light collection and excellent image quality[7]. Such high-resolution imaging underlies many methods in quantum control and quantum information science[5,6], such as quantum networks[8], fundamental atom–light interactions[9] and the sensing of small-scale forces[10]. Individual atoms in particular have been resolved and imaged for many such applications[11–18], with performance that depends critically on minimizing misalignments and optical aberrations from intervening optical surfaces such as a vacuum window.

In this Article we develop a general method for suppressing aberrations by characterizing and adapting the imaging system, and report the highest-performance optical imaging of an isolated atom to date. We image a single ^{174}Yb$^+$ atomic ion with a position sensitivity of ~0.5 nm Hz$^{-1/2}$ for averaging times less than 0.1 s, observe a minimum uncertainty of 1.7(3) nm and obtain direct measurements of the nanoscale dynamics of atomic motion. Complete knowledge of the wavefront distortions is obtained by applying the Zernike expansion of the point spread function, and we adapt this information to correct aberrations and misalignments. The generality of the described work paves the way for adaptive optimal imaging in many other quantum optical systems as well as other contexts, such as biological microscopy or astronomy.

Experimental apparatus

The atomic imaging system is presented in Fig. 1 (see Supplementary Section I). A single ^{174}Yb$^+$ ion is confined in vacuum using a linear Paul trap[6,19] with three-dimensional harmonic oscillation frequencies $(\omega_x, \omega_y, \omega_z)/2\pi = (1, 1.2, 0.8)$ MHz. Laser light at a wavelength of $\lambda = 369.5$ nm is incident on the ion and resonantly excites the $^2S_{1/2} \rightarrow {}^2P_{1/2}$ cycling transition (radiative linewidth of $\gamma/2\pi = 20$ MHz) as shown in Fig. 1a. The ion is laser-cooled and localized in each of the three dimensions of position to $\Delta x = \sqrt{(2\bar{n}+1)}x_0$, where $x_0 = \sqrt{\hbar/2m\omega_x} \approx 5$ nm is the zero-point spread, $\bar{n}$ is the mean thermal vibrational occupation number along each of the dimensions of motion, and m is the atomic mass[19]. For Doppler laser cooling with the cooling laser at an oblique angle to all directions of motion, $\bar{n} \approx \gamma/2\omega_x \sim 10$, so $\Delta x \sim 20$ nm $\ll \lambda$, and the trapped ion acts as an excellent approximation to a point source.

The isotropic fluorescence from the atom at $\lambda = 369.5$ nm is transmitted through a vacuum viewport and collected by an objective lens of numerical aperture NA = 0.6 with ×10 magnification[15] (Fig. 1b). The intermediate image passes through a pinhole that spatially filters light from background sources. Additional magnification is provided by a second stage lens that forms an image at the face of an electron-multiplying charge-coupled-device (EMCCD) camera (Fig. 1c). The objective lens is mounted on a precision five-axis alignment stage to compensate for comatic aberrations, and cylindrical optics are inserted after the magnifier lens to compensate for astigmatic aberrations.

Aberration retrieval and suppression

The measured spatial distribution of the image is the point spread function (PSF)[20], which contains information about the ultimate resolution achievable in an imaging system and is the building block for more complex image formation through deconvolution techniques. The PSF can be decomposed into Zernike polynomials $Z_n^m(\rho, \theta)$ (see Methods) in space

$$\text{PSF}(\rho, \theta) = \left| \mathcal{F}\left\{ \exp\left(-ik \sum_{m,n} c_n^m Z_n^m(\rho, \theta) \right) \right\} \right|^2 \quad (1)$$

where $\mathcal{F}\{\ \}$ is the Fourier transform operator, $k = 2\pi/\lambda$ is the wavenumber and the c_n^m coefficients are contributions of each Zernike component defined in the polar coordinates ρ and θ. The c_n^m coefficients correspond to particular optical aberrations, so detailed characterization of the imaging system follows from the retrieval of the sign and magnitude of these coefficients.

Decomposing an image into Zernike polynomials relies on numerical algorithms[21,22] or semi-analytical calculations[23]. Here, we obtain a full aberration characterization by using a least-squares fit to the measured data, using the c_n^m coefficients and the exit pupil radius as fitting parameters. Although this method omits consideration of vector (polarization) effects, it remains a generally applicable technique because these effects can be neglected at numerical apertures above 0.6 NA (ref. 24).

Figure 2 shows six single-shot images of a single ^{174}Yb$^+$ ion. The images in Fig. 2a–c were taken during alignment and in Fig. 2d–f were taken at different distances from the focal plane of the optimally aligned system. The images were integrated for ~0.5 s,

Joint Quantum Institute, Joint Center for Quantum Information and Computer Science, and Department of Physics, University of Maryland, College Park, Maryland 20742, USA. *e-mail: jwongcam@umd.edu
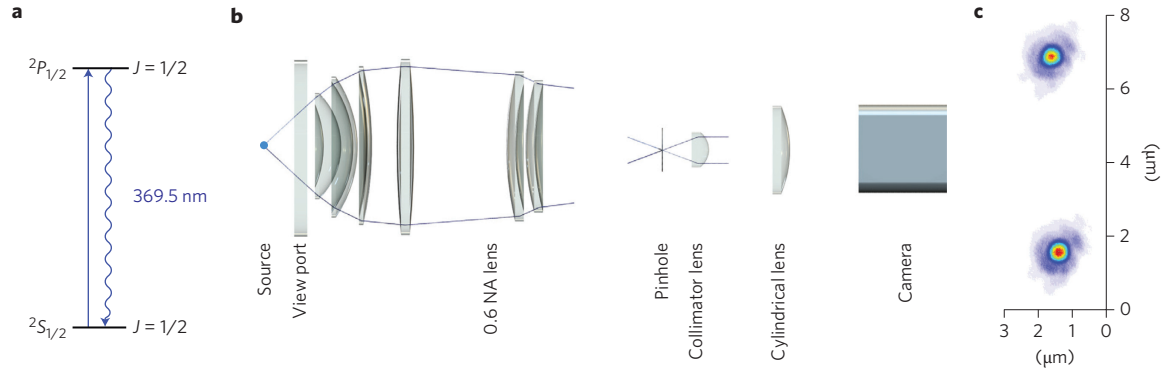
1

Figure 1 | Schematic of the imaging system. a, Atomic energy diagram for ^{174}Yb$^+$. The atom is excited with laser radiation at 369.5 nm, driving the $^2S_{1/2} \rightarrow {}^2P_{1/2}$ cycling transition, and the resulting fluorescence is collected by the imaging system. **b**, Transverse cut of the optical set-up depicting the source, vacuum window, 0.6 NA objective lens, pinhole, short-focal-length lens, cylindrical lens and camera. **c**, Image of two atomic ions separated by 5 μm.

collecting $\sim 7 \times 10^5$ photons and fitted according to equation (1) to a linear superposition of the first 12 Zernike polynomial basis functions. The overall fitting function was then smoothed by convolving with a Gaussian function that best fit the data and accounted for spatial drifts over long exposures. The Gaussian function parameters were added to the fitting algorithm and are only important for integration times longer than 0.2 s (see next section and Supplementary Section II). We found that the optimal image (Fig. 2f) has a characteristic radius of $\rho_0 = 363(18)$ nm, consistent with the diffraction-limited Airy radius of $\rho_0 = 0.61\lambda/\text{NA} = 375.1$ nm given the system numerical aperture.

Based on the one-to-one mapping of the Zernike polynomials to optical aberrations, we plotted an aberration budget, which shows the leading order aberration contributions to each of the images. For example, the contribution of the dominating negative (positive) defocus term of Fig. 2d (Fig. 2e) shows that we can map axial displacement on a transverse image distribution, with the position of best focus shown in Fig. 2f. Moreover, a contribution of the comatic aberration indicates angular tilt errors, and non-zero values of astigmatism indicate anisotropic foci in the system, as seen in Fig. 2a–c.

Fitting results show parameter uncertainties on the order of 1 nm (Supplementary Section II), providing a full quantitative basis for analysing systems that rely on aberrations to extract information on particle dynamics. Examples of these experiments involve three-dimensional off-focus tracking[25] and imaging of atoms arranged in 3D lattices[26]. Although we describe an atomic emitter, this method can also be applied to the imaging of microbiological test samples (see Supplementary Section IV for an example).

Position sensitivity

The precision of measuring atomic position is dependent on the imaging system light collection and quality. As a result of the optical aberration characterization, even if it is not possible to directly correct the aberrations in the imaging system by alignment, it is feasible to post-process and actively feed back the aberrated image and obtain a diffraction-limited performance through a digital filter with the phase information of the Zernike expansion. In this experiment we correct the aberrations by direct alignment (Supplementary Section I).

We measured the sensitivity to the position by taking N images at 1 ms exposure time, binning them over total time duration intervals τ and calculating the Allan variance of the central position[27]:

$$\sigma^2(\tau) = \frac{1}{2(M-1)} \sum_{n=1}^{M-1} (y_{n+1} - y_n)^2 \tag{2}$$

where M is the number of samples per bin and y_n is the centroid of the ion image integrated over time τ. Each image was integrated along one direction and fit to a one-dimensional Gaussian linear count density function. The same procedure taken at different times τ leads to a curve of position uncertainty δ_x versus integration time, as shown in Fig. 3. The data are corrected for a dead time of 5 ms between each 1 ms frame, allowing for state preparation and laser cooling (see Methods and refs 27,28).

The net position sensitivity is a quadrature of three main (uncorrelated) sources of uncertainty: shot noise, pixelation and background noise[29,30]:

$$\delta_x = \sqrt{\frac{2\rho_0^2}{R_0\tau} + \frac{l_{\text{P}}^2}{12R_0\tau} + \frac{16\pi\rho_0^4 b}{R_0^2\tau^2}} \tag{3}$$

where $b \approx 0.07$ is the mean background count rate per pixel, $l_{\text{P}} \approx 33$ nm is the pixel size referred to the object (image pixel size divided by the magnification) and $R_0 = \eta_{\text{D}}F\gamma/2$ is the maximum (saturated) measured fluorescence count rate from the atom, $F \approx 10\%$ is the solid angle fraction of fluorescence collected and $\eta_{\text{D}} \approx 25\%$ is the quantum efficiency of the camera. Finite pixel size and background counts have negligible impact on the measured position sensitivity in this experiment. The observed sensitivity of ~ 0.5 nm Hz$^{-1/2}$ at small integration times is somewhat higher than the expected level of shot noise (shown as the blue line in Fig. 3) and is consistent with observed super-Poissonian noise on the camera. We measured a minimum uncertainty of $\delta_x \approx 1.7(3)$ nm at an integration time of $\tau = 0.2$ s. For longer integration times, drifts in the relative position between the optical objective and the trapped ion degrade the position uncertainty as shown in Fig. 3 and with simple mechanical improvements in the imaging set-up the resolution can probably be pushed well below 1 nm.

Given this uncertainty in the position of the harmonically bound ion, the sensitivity to detecting external forces is $\delta F = m\omega_x^2\delta_x$. For a single ^{174}Yb$^+$ ion with $\omega_x/2\pi = 10$ kHz, this would correspond to a force sensitivity in the yoctonewton (10^{-24} N) scale, or an electric field at the μV cm^{-1} scale. Unlike earlier work[10], this imaging force sensor applies to single ions and does not require the resolution of optical sidebands.

Sensing of RF-induced micromotion position

Confinement of atomic ions in a Paul trap is achieved by means of oscillating RF electric field gradients that create a harmonic ponderomotive potential[31]. In the presence of a static uniform electric field E, the ion acquires a 'micromotion' modulation in position $x(t) = X_\mu \sin \Omega t$ to first order in the pseudopotential
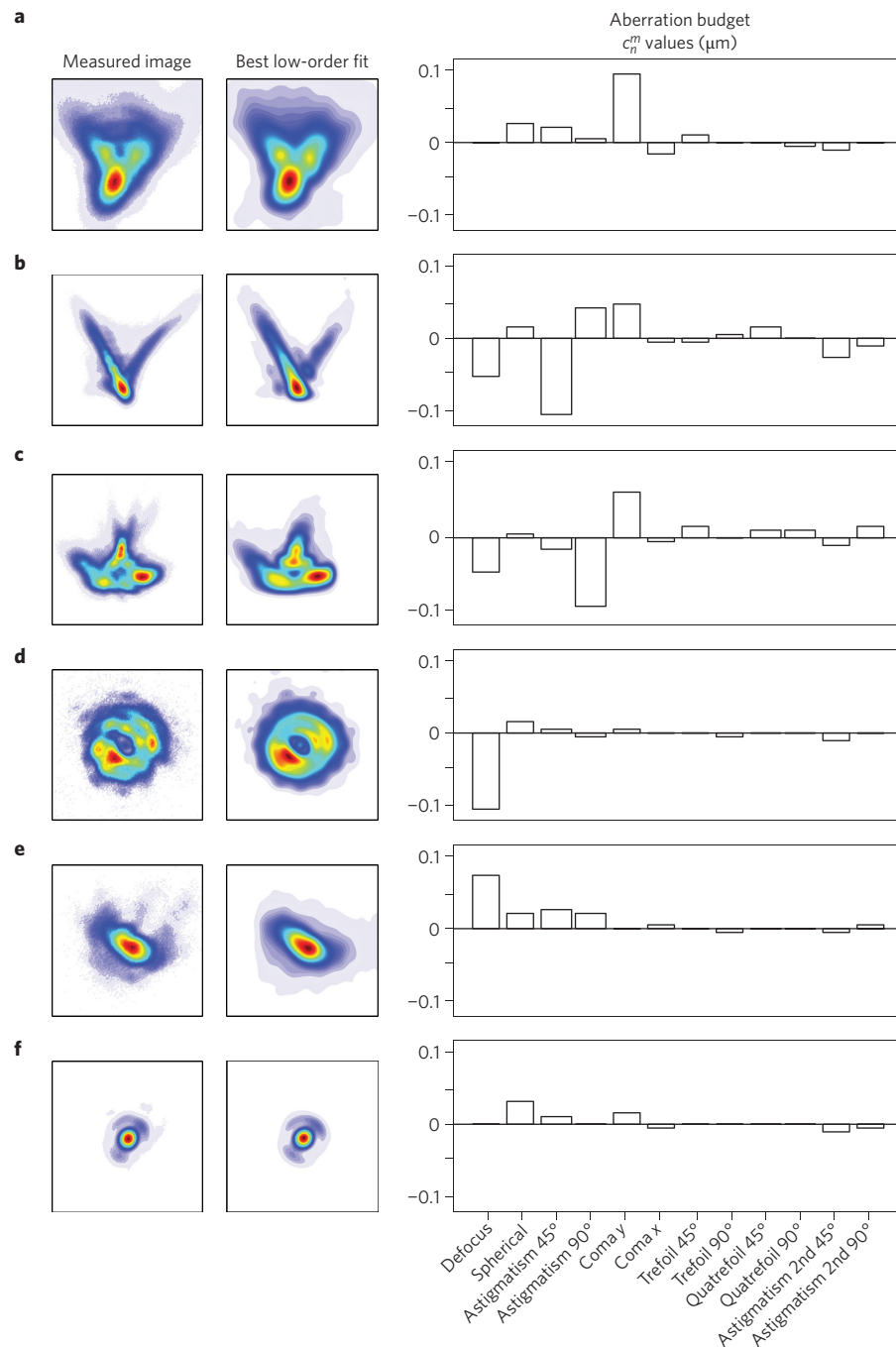
Figure 2 | Aberration retrieval results. a–c, Single-shot images of the misaligned system. **d–f,** The optimally aligned system at various distances from the focal plane, with the best focus shown in **f**. In **d,e,** a high contribution from the defocus term is evident, with low contributions of astigmatism and coma (right). Large contributions of coma and astigmatism (**a–c**) are corrected with a five-axis stage and cylindrical lens (Supplementary Section I). The goodness of fit obtained for these examples approaches unity at coefficients of determination of 0.989, 0.965, 0.958, 0.957, 0.983 and 0.994 for images **a–f**, respectively. These images are integrated for ~0.5 s. Further analysis of the coefficients error bars is provided in Supplementary Section II.

approximation[19,31], where Ω is the drive frequency of the RF trapping field (~17 MHz in this experiment) and $X_\mu = \sqrt{2eE/(m\Omega\omega)}$ is the micromotion amplitude.

The conventional approach for sensing micromotion is based on the first-order Doppler modulation in the scattering of light from a laser beam of wavenumber k propagating along the micromotion velocity[32] (Fig. 4a). The correlation between the photon arrival times (measured with a photomultiplier tube) and the micromotion velocity is obtained with a time-to-digital converter. With the

excitation laser red-detuned from resonance of order γ and for small levels of micromotion $kX_\mu \ll 1$, the measured fluorescence signal takes the form[33]

$$R(t) = \alpha R_0 + \beta R_0 \left(\frac{kX_\mu\Omega}{\gamma} \right) \cos \Omega t \qquad (4)$$

where $\alpha, \beta \leq 1$ are dimensionless constants that depend on the precise detuning and intensity of the excitation laser[33].
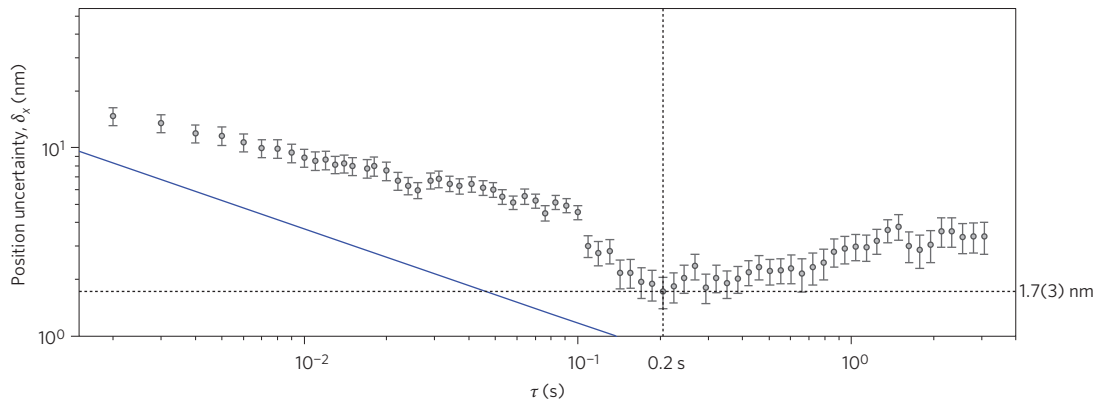
Figure 3 | Measured position uncertainty δ_x of the trapped ion centroid position versus image integration time τ. The blue line shows the expected uncertainty limited by photon counting shot noise in the imaging system. A sensitivity of ~ 0.5 nm Hz$^{-1/2}$ is measured for $\tau < 0.1$ s, which is approximately three times higher than the shot noise, presumably from camera noise. The ultimate position sensitivity is found to be 1.7(3) nm at $\tau = 0.2$ s. These measurements include small corrections for dead time bias, as described in the Methods. Error bars on each point indicate root-mean-square error.

To also sense the direct position sensitivity to motion, we spatially mask the ion image with a sharp edge aperture, normal to the x direction of motion. The mask position can be adjusted from, effectively, $a = -\infty$ (completely exposed) to $a = +\infty$ (completely masked), with $a = 0$ covering exactly half of the image. The total fluorescence behind the mask is then the integrated fluorescence behind the exposed area:

$$R(a, t) = \alpha F(a) R_0$$
$$+ \beta F(a) R_0 \left(\frac{k X_\mu \Omega}{\gamma} \right) \cos \Omega t \qquad (5)$$
$$+ \alpha R_0 \frac{X_\mu}{\sigma \sqrt{\pi}} e^{-a^2/2\sigma^2} \sin \Omega t$$

where we assume a Gaussian image distribution in space with root-mean-square radius $\sigma = 0.36 \rho_0$ and the scale of the mask position a is referred to the object. The cumulative distribution function is $F(x) = [1 - \mathrm{erf}(x/\sigma\sqrt{2})]/2$.

We extract the two quadratures of the modulated fluorescence from equation (5) by performing sine and cosine transforms of the data. The phases of the modulated signal are calibrated by opening the aperture ($a = -\infty$) and taking the modulation as proportional to $\cos \Omega t$.

Figure 4b shows the position ($\sin \Omega t$) and velocity ($\cos \Omega t$) quadrature amplitudes (normalized to the amplitude at $a = -\infty$) as the mask position is scanned. Based on the observed velocity-induced modulation in the count rate with full exposure ($a = -\infty$), we infer a micromotion amplitude of $X_\mu \sim 20$ nm. As the mask is scanned along x, a position-dependent modulation in the fluorescence rate arises, reaching a maximum level at $a = 0$. The absolute level of this position-dependent modulation is observed to be 15 times smaller than expected from equation (5). This may be due to slow drifts in the relative position of the ion with respect to the mask— a fluctuation of just 30 nm over the 300 s integration time required to obtain sufficient signal-to-noise ratio in the measurement would explain the observed reduction in the modulation.
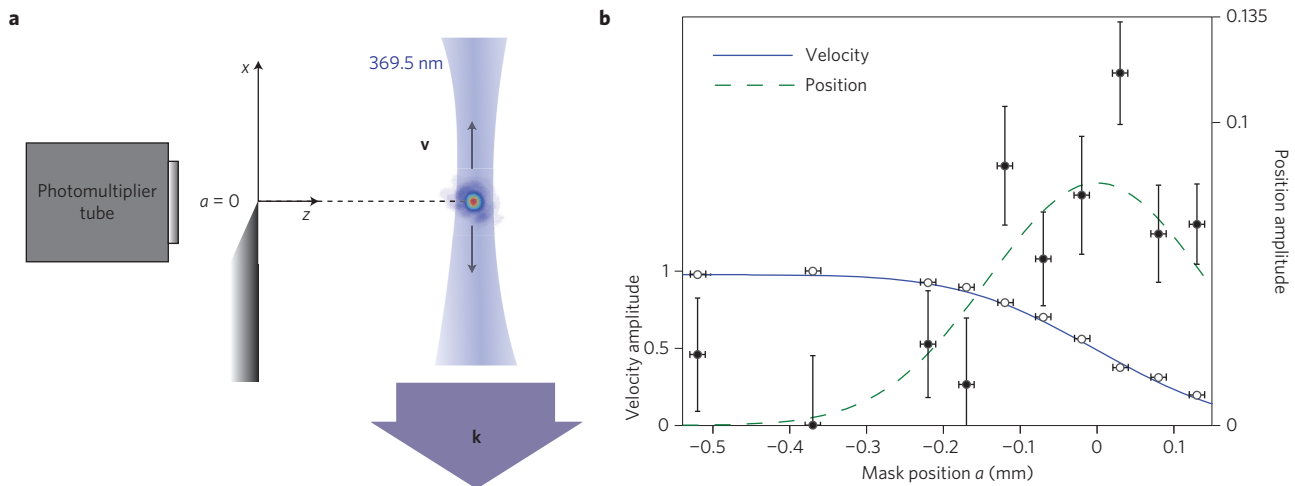

Figure 4 | Micromotion position measurement. a, The ion's velocity **v** (solid black arrows) is colinear with the direction **k** of the detection light, taken to be the x axis. Fluorescence is modulated from the micromotion of the ion along x by the first-order Doppler effect as well as the obscuration by a mask with variable position a along the x axis. **b,** Contributions of the velocity (left y axis) and position (right y axis) of a single atom when a mask is scanned along one transversal direction x. The solid and dashed lines depict fits to the data for the velocity and position components, respectively, of equation (5), given respectively by the cosine and sine terms alone. All values are normalized with the signal amplitude at $a = -\infty$. Horizontal error bars represent the uncertainty of the scanning stage (0.01 mm) and vertical errors are computed from the uncertainty propagation using equation (5).

Outlook

In the single-atom emitter presented here, ultimate position localization to the level of ångströms (10^{-10} m) should be possible for longer integration times, when drifts slower than 0.2 s are eliminated or actively corrected. Drifts may be reduced by further isolating the vacuum chamber from the environment and stabilizing the relative position between the sample and the objective. Because we obtain information of the centroid position, the zero-point ion motion does not affect these measurements.

More generally, the isolation and correction of wavefront distortions by fitting intensity images can be extended to the adaptive imaging of a variety of source objects. If the fluorescence from the emitter is incoherent, then imaging errors should not accumulate and images from multiple emitters localized in distinct regions of space could be corrected. This technique can also be used for the optimization of laser output cavity spatial modes[34]. Most misalignments provide an unambiguous signature in the image decomposition, but for certain symmetric misalignments such as axial displacements about the focus for single atoms, introducing additional aberrations such as astigmatism[26] or coma will yield a unique fit. Given sufficient emitter brightness, active shot-to-shot adjustments and feedback to appropriate optical elements should allow the continuous optimization of image quality. The bandwidth of this type of adaptive imaging would be limited by the speed of the correction elements and the computing time for numerically extracting the error signal (this is ~1 s in our experiment).

Methods

Methods and any associated references are available in the online version of the paper.

References

1. Moerner, W. Nobel lecture. Single-molecule spectroscopy, imaging, and photocontrol: foundations for super-resolution microscopy. *Rev. Mod. Phys.* **87**, 1183–1212 (2015).
2. Betzig, E. Nobel lecture. Single molecules, cells, and super-resolution optics. *Rev. Mod. Phys.* **87**, 1153–1168 (2015).
3. Eva, R. *et al.* STED microscopy reveals crystal colour centres. *Nature Photon.* **3**, 144–147 (2009).
4. Betzig, E. *et al.* Imaging intracellular fluorescent proteins at nanometer resolution. *Science* **313**, 1642–1645 (2006).
5. Bakr, W., Gillen, J., Peng, A., Fölling, S. & Greiner, M. A quantum gas microscope for detecting single atoms in a Hubbard-regime optical lattice. *Nature* **462**, 74–77 (2009).
6. Blatt, R. & Wineland, D. Entangled states of trapped atomic ions. *Nature* **453**, 1008–1015 (2008).
7. Hell, S. Nobel lecture. Nanoscopy with freely propagating light. *Rev. Mod. Phys.* **87**, 1169–1182 (2015).
8. Monroe, C. *et al.* Large-scale modular quantum-computer architecture with atomic memory and photonic interconnects. *Phys. Rev. A* **89**, 022317 (2014).
9. Eschner, J., Raab, Ch., Schmidt-Kaler, F. & Blatt, R. Light interference from single atoms and their mirror images. *Nature* **413**, 495–498 (2001).
10. Biercuk, M., Uys, H., Britton, J., VanDevender, A. & Bollinger, J. Ultrasensitive detection of force and displacement using trapped ions. *Nature Nanotech.* **5**, 646–650 (2010).
11. Schlosser, N., Reymond, G., Protsenko, I. & Grangier, P. Sub-Poissonian loading of single atoms in a microscopic dipole trap. *Nature* **411**, 1024–1027 (2001).
12. Karpa, L., Bylinskii, A., Gangloff, D., Cetina, M. & Vuletić, V. Suppression of ion transport due to long-lived subwavelength localization by an optical lattice. *Phys. Rev. Lett.* **111**, 163002 (2013).
13. Schmiegelow, C. *et al.* Phase-stable free-space optical lattices for trapped ions. *Phys. Rev. Lett.* **116**, 033002 (2016).
14. Alberti, A. *et al.* Super-resolution microscopy of single atoms in optical lattices. *New J. Phys.* **18**, 053010 (2016).
15. Noek, R. *et al.* High speed, high fidelity detection of an atomic hyperfine qubit. *Opt. Lett.* **38**, 4735–4738 (2013).
16. Burrell, A., Szwer, D., Webster, S. & Lucas, D. Scalable simultaneous multiqubit readout with 99.99% single-shot fidelity. *Phys. Rev. A* **81**, 040302 (2010).
17. Streed, E., Norton, B., Jechow, A., Weinhold, T. & Kielpinski, D. Imaging of trapped ions with a microfabricated optic for quantum information processing. *Phys. Rev. Lett.* **106**, 010502 (2011).
18. Shu, G., Chou, C., Kurz, N., Dietrich, M. & Blinov, B. Efficient fluorescence collection and ion imaging with the 'tack' ion trap. *J. Opt. Soc. Am. B* **28**, 2865–2870 (2011).
19. Leibfried, D., Blatt, R., Monroe, C. & Wineland, D. Quantum dynamics of single trapped ions. *Rev. Mod. Phys.* **75**, 281–324 (2003).
20. Goodman, J. *Introduction to Fourier Optics* (McGraw-Hill, 1996).
21. Iglesias, I. Parametric wave-aberration retrieval from point-spread function data by use of a pyramidal recursive algorithm. *Appl. Opt.* **37**, 5427–5430 (1998).
22. Barakat, R. & Sandler, B. Determination of the wave-front aberration function from measured values of the point-spread function: a two-dimensional phase retrieval problem. *J. Opt. Soc. Am. A* **9**, 1715–1723 (1992).
23. Avoort, C., Braat, J., Dirksen, P. & Janssen, A. Aberration retrieval from the intensity point-spread function in the focal region using the extended Nijboer–Zernike approach. *J. Mod. Opt.* **52**, 1695–1728 (2005).
24. Novotny, L. & Hecht, B. *Principles of Nano-Optics* (Cambridge Univ. Press, 2006).
25. Speidel, M., Jonáš, A. & Florin, E. Three-dimensional tracking of fluorescent nanoparticles with subnanometer precision by use of off-focus imaging. *Opt. Lett.* **28**, 69–71 (2003).
26. Nelson, K., Li, X. & Weiss, D. Imaging single atoms in a three-dimensional array. *Nature Phys.* **3**, 556–560 (2007).
27. Riley, W. *Handbook of Frequency Stability Analysis* Special Publication 1065 (NIST, 2008).
28. Barnes, J. & Allan, D. *Variances Based on Data with Dead Time Between the Measurements* Technical Note 1318 (NIST, 1990).
29. Thompson, R., Larson, D. & Webb, W. Precise nanometer localization analysis for individual fluorescent probes. *Biophys. J.* **82**, 2775–2783 (2002).
30. Quan, T., Zeng, S. & Huang, Z. Localization capability and limitation of electron-multiplying charge-coupled, scientific complementary metal-oxide semiconductor, and charge-coupled devices for superresolution imaging. *J. Biomed. Opt.* **15**, 066005 (2010).
31. Major, F. & Dehmelt, H. Exchange-collision technique for rf spectroscopy of stored ions. *Phys. Rev.* **170**, 91–107 (1968).
32. Berkeland, D., Miller, J., Bergquist, J., Itano, W. & Wineland, D. Minimization of ion micromotion in a Paul trap. *J. Appl. Phys.* **83**, 5025–5033 (1998).
33. Keller, J., Partner, H., Burgermeister, T. & Mehlstäubler, T. Precise determination of micromotion for trapped-ion optical clocks. *J. Appl. Phys.* **118**, 104501 (2015).
34. Anderson, D. Alignment of resonant optical cavities. *Appl. Opt.* **23**, 2944–2949 (1984).

Author contributions

All authors contributed to the design, construction and carrying out of the experiment, discussed the results and commented on the manuscript. J.D.W.-C. and K.G.J. analysed the data and performed the simulations. J.D.W.-C., K.G.J. and C.M. wrote the manuscript. B.N. and J.M. contributed equally to both the design and construction of the experiment.

Competing financial interests

The authors declare no competing financial interests.

Methods

Aberration characterization. Although optical aberrations can be described in terms of a Taylor expansion of the object height and pupil coordinates, Zernike polynomials $Z_n^m(\rho, \theta)$ are better suited for this because they form an orthogonal basis set of functions on a unit disk. Zernike polynomials are expressed in polar coordinates ρ and θ as[35]

$$Z_n^m(\rho, \theta) = \begin{cases} N_n^m R_n^m(\rho) \cos(m\theta) & \text{for } m \geq 0 \\ N_n^m R_n^m(\rho) \sin(m\theta) & \text{for } m < 0 \end{cases}$$

$$N_n^m = \sqrt{\frac{2(n+1)}{1+\delta_{m0}}}$$

$$R_n^{|m|}(\rho) = \sum_{s=0}^{(n-|m|)/2} \frac{(-1)^s}{s! [(n+|m|)/2 - s]!} \times \frac{(n-s)!}{[(n-|m|)/2 - s]!} \left(\frac{\rho}{\rho_p}\right)^{n-2s} \quad (6)$$

where n is an integer number and m can only take values n, $n-2$, $n-4$, …, $-n$ for each n. The radial coordinate is scaled to the exit pupil radius ρ_p (the radius of the image of the input aperture at the camera). Importantly, each term of this polynomial expansion has a one-to-one relation with a specific kind of aberration.

Given the Zernike expansion of a wavefront, we can calculate its deviation from a perfect wavefront using the c_n^m coefficients of equation (1).

Dead time corrections. Dead times were corrected using the Allan B-functions[28] (defined in Supplementary Section V):

$$\sigma^2(\tau) = \frac{\sigma^2(2, \mathcal{M}T_0, \mathcal{M}\tau_0)}{B_3(\mu)B_2(\mu)} \quad (7)$$

where μ is the noise model coefficient, in the range $-1 < \mu < 1$, M is the binning parameter, T_0 is the time between data acquisitions, and τ_0 is the sampling time. Dead times are then defined as $t_{dead} = T_0 - \tau_0$ for single acquisition times. The integration time for the Allan variance is $\tau = M\tau_0$. The noise model μ upon which the B-functions depend at each τ are found solving

$$\frac{B_1(\mu)}{B_3(\mu)} = \frac{\sigma^2(N, T, \tau)}{\sigma^2(2, \mathcal{M}T_0, \mathcal{M}\tau_0)} \quad (8)$$

for μ, with $\sigma^2(N, T, \tau)$ defined as the standard variance.

Reference

35. Wyant, J. & Creath, K. *Applied Optics and Optical Engineering* Vol. XI (Academic, 1992).